

铁基非晶纳米晶涂层组织与冲蚀性能分析

梁秀兵¹, 程江波^{1,2}, 白金元¹, 陈永雄¹, 徐滨士¹

(1. 装甲兵工程学院 装备再制造技术国防科技重点实验室, 北京 100072;

2. 上海交通大学 材料科学与工程学院, 上海 200240)

摘 要: 利用高速电弧喷涂技术成功制备了 FeCrBSiMnNbY 系和 FeBSiNbCr 系非晶纳米晶涂层。采用扫描电镜、X 射线衍射仪等设备对涂层的组织结构进行了表征, 重点分析了非晶的形成机制, 并对涂层的高温冲蚀性能进行了研究。结果表明, FeCrBSiMnNbY 系和 FeBSiNbCr 系涂层的组织主要由非晶相和 α (Fe, Cr) 相纳米晶组成; 两种涂层结构致密, 组织均匀, 孔隙率含量分别为 1.7% 和 1.2%; FeBSiNbCr 系非晶纳米晶涂层具有良好的耐高温冲蚀性能, 随着攻角增加, 涂层冲蚀率随之增加; 冲蚀温度升高, 涂层耐冲蚀性能也随着提高。

关键词: 非晶纳米晶; 涂层; 高温冲蚀

中图分类号: TG174.4 **文献标识码:** A **文章编号:** 0253-360X(2009)02-0061-04



梁秀兵

0 序 言

非晶纳米晶合金作为一种新型材料, 具有高的强度、韧性、良好耐磨和耐蚀性能等特点, 是当前国际材料研究领域的热点之一^[1]。利用纳米化技术提高材料的耐磨性能, 利用非晶化技术提高材料的耐蚀性能, 将纳米化技术与非晶化技术结合, 制备耐蚀耐磨综合性能优异的非晶纳米晶材料具有广阔的应用背景。

目前这些材料仍然还没有大范围推广应用, 主要因素是制备工艺过程难以控制, 其应用主要被限制在薄带、细丝、粉末等低维度形状上。相对而言, 非晶纳米晶涂层的制备过程就比较容易实现。采用热喷涂技术来制备非晶纳米晶涂层是对其制备技术的新开拓。目前, 用于制备非晶纳米晶涂层的热喷涂技术主要集中在等离子喷涂^[2]和高速火焰喷涂^[3]非晶材料获得。相对于这些技术而言, 电弧喷涂技术是一种低成本、简单高效的涂层制备技术。然而, 采用电弧喷涂技术制备非晶纳米晶涂层方面的工作在国内外只有很少的报道。

文中利用高速电弧喷涂技术在钢基体上制备了不同体系的非晶纳米晶涂层, 并对其组织结构进行了表征和冲蚀性能进行了研究, 为其实际应用打下

了基础。

1 试验方法

喷涂材料为自行开发的 $\phi 2$ mm 两种粉芯丝材, 基体材料为 45 钢。喷涂前, 基材表面用丙酮清洗除油净化, 进行喷砂预处理, 完毕后立即喷涂。喷涂的主要工艺参数为喷涂电压 36 V, 送丝速度 2.8 m/min, 喷涂距离 200 mm, 气压 0.7 MPa。采用装备再制造技术国防科技重点实验室的自动化高速电弧喷涂系统制备涂层。

试验后, 采用 D8 型 X 射线衍射仪对涂层进行相结构分析, 利用 Quanta 200 型环境扫描电镜分析涂层截面的显微结构和表面冲蚀形貌。采用 HVS-1000 型显微硬度计测量涂层表面以及截面的显微硬度, 载荷为 1.98 N, 加载时间 15 s。

采用 GM/CS2MS 型高温冲蚀磨损试验装置测试涂层的冲蚀性能, 试验条件为大气环境, 从室温到 650 $^{\circ}\text{C}$, 磨粒为石英砂, 质量为 375 g, 冲蚀速度 62 m/s, 冲击角度 30 $^{\circ}$ 和 90 $^{\circ}$, 冲蚀时间 30 min。

2 试验结果及分析

2.1 涂层的组织结构

图 1 为非晶纳米晶涂层截面组织形貌。两种系列的涂层组织均匀, 结构致密, 涂层与基体以及层与

层之间结合完好,只有少量的孔隙分布于涂层中,整个涂层几乎没有裂纹.其中 FeBSiNbCr 系涂层截面要比 FeCrBSiMnNbY 系涂层更加致密.两种系列涂层的孔隙率均比较低,利用图像分析软件测量涂层的孔隙率分别为图 1a 中 1.7%和图 1b 中 1.2%. FeCrBSiMnNbY 系涂层主要的化学组成(质量分数,%)为 Fe_{64.82}Cr_{9.23}B_{20.69}Si_{1.9}Mn_{1.01}Nb_{1.8}Y_{0.55}; FeBSiNbCr 系涂层的主要化学组成(质量分数,%)为 Fe_{65.8}B_{26.88}Si_{2.02}Nb_{2.29}Cr_{3.01}.

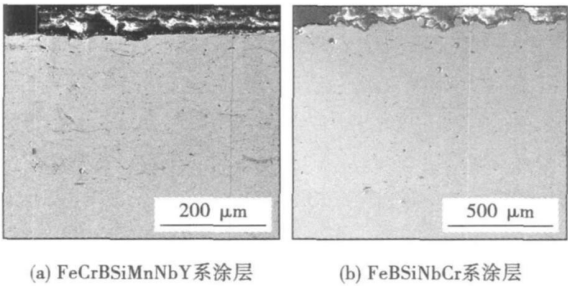


图 1 涂层的截面形貌
Fig 1 SEM images of coatings

图 2 为两种涂层的 XRD 图.在两种涂层的 XRD 曲线 $2\theta=45^\circ$ 处均出现了一个漫散射峰,说明在喷涂过程中形成了非晶相.但是两种涂层中还存在少量的晶化峰,证明涂层在沉积过程中形成了少量的纳米晶,涂层的组织结构由非晶相和 $\alpha(\text{Fe,Cr})$ 纳米晶组成,通过 Verdon 方法对 XRD 图谱进行 Pseudo-Voigt 函数拟合,计算得到 FeCrBSiMnNbY 系涂层中非晶相的含量为 63.2%; FeBSiNbCr 系涂层非晶相含量为 71.3%. 利用谢乐公式计算可知涂层中纳米晶的尺寸为 17 nm 和 11 nm. 另外,两种系列的涂层中没有氧化物峰存在,说明涂层在沉积过程中很少发生氧化,机理尚需深入研究.

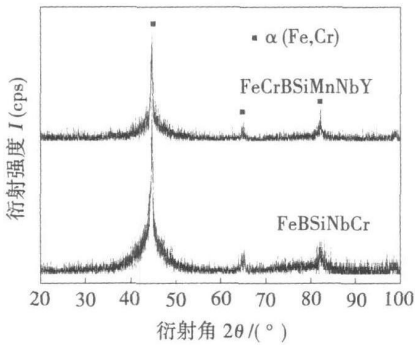


图 2 涂层的 XRD 图谱
Fig. 2 XRD patterns of coatings

两种体系的涂层在喷涂过程中形成了大量非晶相,这是因为在喷涂过程中,熔融的液态粒子的瞬间凝固速率约为 $10^5 \text{ K/s}^{[4]}$,这为非晶的形成提供了条件. FeCrBSiMnNbY 系和 FeBSiNbCr 系材料均具有较高的非晶形成能力,其组成中不同的原子尺寸和混合热焓在非晶的形成过程中起了很重要的作用^[5]. 材料组成中类金属(B, Si)含量的增加也会增强非晶的形成与稳定性. 加入小原子尺寸的元素使体系原子尺寸差增大,混乱度增强、长程无序性增加. B 和 Si 元素的加入可以降低合金的熔点,还能扩大固相和液相之间的距离. Y 和 Nb 元素作为大原子($Y>Nb>Cr>Mn>Fe>Si>B$)添加到合金当中时,能够与周围彼此约束的近邻原子包括基体原子和小原子形成类似网状结构或骨架结构. 这种结构的形成能够进一步阻碍原子的扩散或者原子团的迁移,使原子的有序化程度降低;同时非晶基体上的这种骨架结构能够增强过冷熔体的稳定性,进一步抑制了晶体相的形核和长大,增加了非晶相形成的倾向性. 另一方面, Fe-B, Fe-Si, Fe-Cr, Fe-Nb 组成的混合热焓分别为 -11, -18, -1, -16 kJ/mol. Cr-B, Cr-Nb, Nb-Si, B-Nb, Y-Mn, Y-Si 和 Y-Fe 组成的混合热焓分别为 -16, -7, -31, -39, -8, -57, -11 kJ/mol^[6]. 可以看出,随着 Nb, Y 元素的加入使得各组元中混合热焓的负值越来越大. 大的负混合热焓能够加强各组元间的相互反应,促进结构的无序性,增加非晶的形成. 因此非晶合金的形成是快速凝固和合理材料设计相互作用的结果.

图 3 是两种体系涂层的显微硬度随截面分布. 两种涂层均具有较高的硬度. 由于涂层中非晶相含量较高,孔隙率较低,所以 FeBSiNbCr 系涂层的硬度要比 FeCrBSiMnNbY 系涂层高.

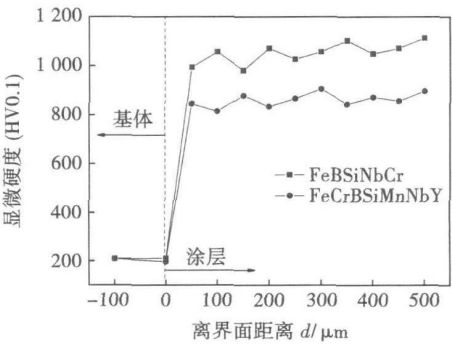


图 3 涂层的显微硬度
Fig 3 Microhardness profiles of coatings

2. 2 攻角对非晶纳米晶涂层冲蚀性能的影响

图 4 为非晶纳米晶涂层和 45 钢在常温时不同

攻角下的气-砂冲蚀磨损曲线。可以看出, 非晶纳米晶涂层的耐冲蚀性能要高于 45 钢。涂层在 30° 的冲蚀率要低于 90° 攻角的冲蚀率; 而基体在大攻角下其冲蚀率要低于小攻角的冲蚀率。FeBSiNbCr 系涂层具有良好的抗冲蚀性能。

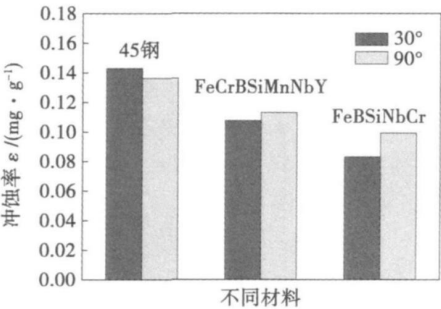


图 4 常温时不同攻角下涂层和 45 钢冲蚀率的分布
Fig. 4 Erosion rates of amorphous coatings and 45 steel under different impingement angles at room temperature

图 5 是基体和 FeBSiNbCr 系涂层不同攻角的表面冲蚀形貌。图 5a, b 是基体在不同攻角下, 表面冲蚀形貌, 可以看出大量的切削与犁沟存在于冲蚀的表面, 这说明基体的冲蚀特征为塑性冲蚀。FeBSiNbCr 系涂层(图 5c, d)冲蚀后的形貌均呈坑状, 没有切削和犁沟形貌; 其 30° 冲蚀形貌要比 90° 时要平滑, 说明此时材料的损失量较小, 非晶纳米晶涂层的冲蚀特性主要表现为脆性剥落。

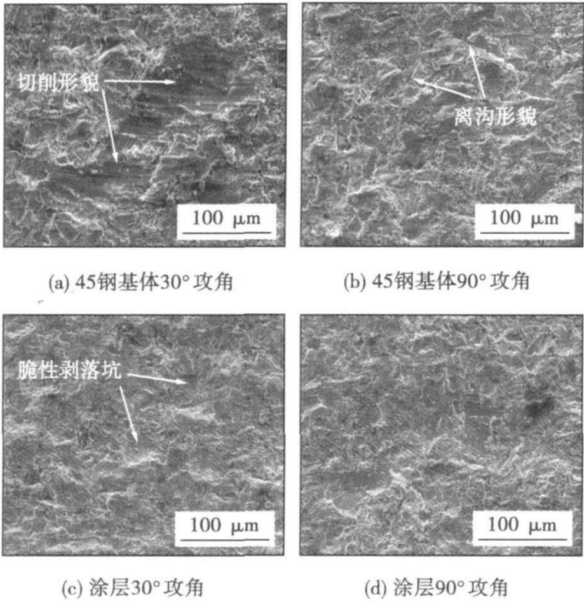


图 5 常温不同攻角基体和涂层(FeBSiNbCr)冲蚀形貌
Fig. 5 SEM surface images of coatings (FeBSiNbCr) under different impingement angles at room temperature

冲蚀率随攻角变化把材料的冲蚀破坏分为两类, 即塑性材料和脆性材料的冲蚀破坏。当粒子的攻角为 20°~30° 时, 典型的塑性材料冲蚀率达到最大值, 而脆性材料的最大冲蚀率出现在冲蚀角度为 90° 处。两种典型冲蚀破坏中攻角与冲蚀率的关系^[7]为

$$\epsilon = A \cos^2 \alpha \sin n \alpha + B \sin^2 \alpha \quad (1)$$

式中: ϵ 为冲蚀率; α 为攻角; n , A , B 为常数; 典型的脆性材料 $A=0$, 塑性材料 $B=0$, $n=\alpha\pi/2$ 。由于非晶纳米晶涂层的脆性相对较大, 因此在冲蚀过程中呈现为脆性剥落, 故较小攻角的冲蚀率要低于大攻角。

2.3 温度对非晶纳米晶涂层冲蚀性能的影响

图 6 是非晶纳米晶涂层与 45 钢在 30° 攻角时, 不同温度条件下的冲蚀试验结果。随着温度的升高, 涂层与基体的耐冲蚀性能均随之提高; 涂层的耐冲蚀性能要优于基体。FeBSiNbCr 系涂层具有最好的抗冲蚀性能, 在 650 °C 的高温下, FeBSiNbCr 系涂层甚至出现了冲蚀增重现象。

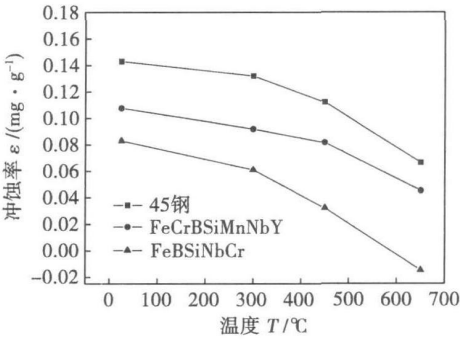


图 6 30° 攻角不同温度涂层和基体冲蚀率的分布
Fig. 6 Erosion rates of coatings and 45 steel at 30° impingement angles

分析发现, 高温下的冲蚀增重的原因如下^[8]。
(1) 在高温下, 形状尖锐的冲蚀用石英磨粒划过涂层的表面, 使一部分氧化膜由于和基体塑性变形不协调而开裂和剥落, 从而使新鲜涂层合金暴露出来。涂层合金容易氧化促进损伤氧化膜的愈合; 同时, 涂层合金由于发生塑性变形, 化学位升高, 活性增大, 使氧化加速, 表现为涂层增重。当磨粒连续不断地冲击涂层表面时, 涂层表面氧化膜厚度增加的速率, 高于氧化膜的破裂去除和涂层合金的损耗速率时, 就表现出涂层增重趋势。
(2) 当磨粒连续不断地冲击涂层表面时, 随着氧化物的生成, 大量的磨粒会残留在涂层的表面, 从而导致涂层的增重。
(3) 随着温度的不断升高, 非晶有向纳米晶转变的趋势, 如

图 7 所示, 涂层 XRD 曲线的散漫峰逐渐变窄, 强度不断升高, 从而使得纳米晶形成. 经谢乐公式计算, 随着温度的升高, 涂层中纳米晶颗粒的大小依次为 11, 17, 32 nm. 纳米尺寸的晶粒析出, 对涂层起到弥散强化的作用, 增强了涂层的抗冲蚀性能.

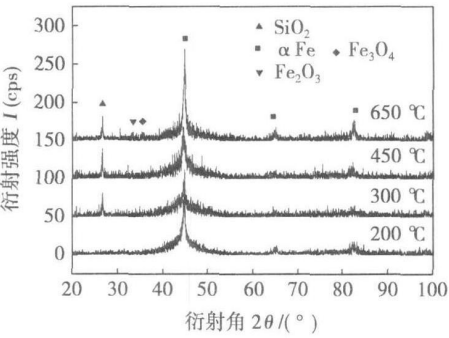


图 7 FeBSiNbCr 系涂层冲蚀后 XRD 图谱
Fig. 7 XRD patterns of FeBSiNbCr coatings

图 8 是不同温度下 FeBSiNbCr 系涂层的冲蚀形貌. 常温下涂层的冲蚀形貌主要表征为冲蚀坑, 其机理主要为脆性剥落; 当温度升高到 450 °C 时, 涂层的冲蚀形貌中出现了犁沟, 如图 8c 箭头所示, 表明涂层的冲蚀机理发生了改变, 由脆性剥落转变为脆性剥落加塑性切削机制; 随着温度的进一步升高, 这种现象仍然存在; 因此, 涂层在高温下的冲蚀机理为脆性剥落和塑性切削两者并存. 这主要是因为非晶

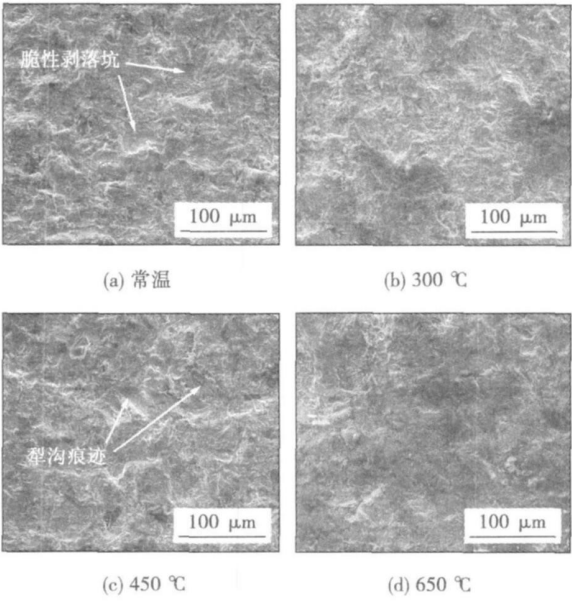


图 8 30° 攻角不同温度下 FeBSiNbCr 系涂层的冲蚀形貌
Fig. 8 SEM images of FeBSiNbCr coatings as function of temperature at 30° impingement angles

相是亚稳相, 其自由能较高, 随着温度的升高, 有向晶体转变的趋势. 涂层发生晶化, 使得涂层的塑性性能逐渐增强, 因此出现了塑性切削. 而且随着温度的升高, 涂层的冲蚀形貌越来越平滑, 说明涂层在冲蚀过程中损失量很少, 因此涂层的冲蚀率逐渐降低.

3 结 论

- (1) 利用电弧喷涂技术在 45 钢基体上制备了 FeCrBSiMnNbY 系和 FeBSiNbCr 系非晶纳米晶涂层. 其组织致密, 结构紧凑, 孔隙率含量低, 分别为 1.7% 和 1.2%.
- (2) 两种系列涂层的组织均由非晶相和 α (Fe, Cr) 纳米晶组成. FeCrBSiMnNbY 系涂层非晶相含量为 63.2%, FeBSiNbCr 系涂层非晶相含量为 71.2%.
- (3) 随着温度的升高, 涂层耐冲蚀性能随之提高; 冲蚀角度的增加, 涂层的冲蚀率增加. 非晶纳米晶涂层在常温下冲蚀机理表征为脆性剥落; 随着温度的升高, 其冲蚀机理由脆性剥落转变为塑性切削和脆性剥落两者并存. FeBSiNbCr 系非晶纳米晶涂层具有良好的抗冲蚀性能.

参考文献:

[1] Schuh C A, Hufragel T C, Ramanurty U. Mechanical behavior of amorphous alloys[J]. *Acta Materials*, 2007, 55(12): 4067—4109.

[2] Kobayashi A, Yano S, Kimura H, et al. Mechanical property of Fe-base metallic glass coating formed by gas tunnel type plasma spraying[J]. *Surface and Coatings Technology*, 2008, 202(12): 2513—2518.

[3] Wu Yuping, Lin Pinghua, Chu Chenglin, et al. Cavitation erosion characteristics of a Fe-Cr-Si-B-Mn coating fabricated by high velocity oxy-fuel (HVOF) thermal spray[J]. *Materials Letters*, 2007, 61(8, 9): 1867—1872.

[4] Nerbery A B, Grant P S, Neiser R A. The velocity and temperature of steel droplets during electric arc spraying[J]. *Surface and Coatings Technology*, 2005, 195(1): 91—101.

[5] Liu Dongyan, Gao Wei, Li Zhengwei, et al. Electro-spark deposition of Fe-based amorphous alloy coatings[J]. *Materials Letters*, 2007, 61(1): 165—167.

[6] Boer F R, Boom R, Mattens W C M, et al. Cohesion in metals transition metal alloys[M]. Netherlands: Elsevier Science Publishing Company Inc., 1989.

[7] 刘家浚. 材料磨损原理及其耐磨性[M]. 北京: 清华大学出版社, 1993.

[8] 徐维普. 高速电弧喷涂 Fe-Al/Cr3C2 复合涂层高温性能研究及应用[D]. 上海: 上海交通大学, 2001.

作者简介: 梁秀兵, 男, 1974 年出生, 博士, 副研究员. 主要从事表面工程与再制造关键技术研究. 发表论文 70 余篇.
Email: liangxiubing@yahoo.com.cn

in the multiple submerged arc welding by using Step Acceleration Method.

Key words: step acceleration method; double ellipsoid heat source model; multiple wires submerged arc welding

Numerical simulation of tensile deformation on aluminum alloy FSW lap joints

ZHOU Yanli, LIU Tao, ZHANG Yanhua (School of Mechanical Engineering and Automation, Beijing University of Aeronautics and Astronautics, Beijing 100083, China). p57—60

Abstract: Fracture behaviour of friction stir welded lap joints in 2A12 aluminum alloy was investigated by strength test. The distribution of stress and strain around the crack tip was calculated by finite element method under stretching forces. Analysis results show that plastic deformation occurs first at crack tip and the maximum plastic deformation is found in crack tip region in upper plate which lead to the fracture of heat-affected zone in upper plate.

Key words: aluminum alloy; lap joints; friction stir welding; joint strength

Microstructure and erosion properties of Fe-based amorphous and nanocrystalline coatings

LIANG Xiubing¹, CHENG Jiangbo^{1,2}, BAI Jinyuan¹, Chen Yongxiong¹, XU Binshi¹ (1. National Key Laboratory for Remanufacturing, Academy of Armored Forces Engineering, Beijing 100072, China; 2. School of Materials Science and Engineering, Shanghai Jiaotong University, Shanghai 200240, China). 61—64

Abstract: FeCrBSiMnNbY and FeBSiNbCr amorphous coatings were fabricated by high velocity wire arc spraying process. The microstructure and phase composition of the coatings were characterized by SEM, EDAX and XRD. The formation mechanism of amorphous phase was discussed. The elevated temperature erosion behavior of the coating was also investigated. The results show that the microstructures of both coatings consist of amorphous phase and α (Fe, Cr) nanocrystalline phase. Both of the coatings are fully dense with low porosity of 1.7% and 1.2%, respectively. The coatings exhibit better erosion resistance at lower impact angles. With increasing the erosion temperature, the erosion rates of the coatings decrease. The FeBSiNbCr coating has better elevated temperature erosion resistance than that of the FeCrBSiMnNbY coating.

Key words: amorphous and nanocrystalline; coatings; elevated temperature erosion

Residual stress analysis on the Ti-bioglass coatings produced by high velocity flame spraying

LI Muqin, ZHUANG Minghui, YIN Ke, WANG Jun (Province Key Laboratory Biomaterials, Jiamusi University, Jiamusi 154007, China). 65—67

Abstract: High velocity flame spraying and coating process technology was adopted to spray pure titanium powder with addition of glaze glass (G) on Ti6Al4V substrate. The coatings were crystallized at temperature 700 °C. The residual macro-stress in the coatings was tested by grazing incidence X-ray diffraction (GIXRD). And the result shows that the coating present residual compressive

stress (RCS). The stress is proportional to the content of the glaze glass. The larger particle size, which increased the kinetic energy of the flying particle, produces larger stress. The reason for presenting RCS is that high spray speed and large kinetic energy generated jet impingement which leads to the existence of the RCS. This is helpful to increase the bonding strength of the coatings.

Key words: high velocity flame spraying; bioglass; residual stress; grazing incidence X-ray diffraction

Effect of molybdenum on crack sensibilities of laser cladded NiCrBSi alloy coatings

ZHANG Ping, YUAN Jinping, SUN Lei, ZHAO Junjun (National Key Laboratory for Remanufacturing, Academy of Armored Forces Engineering, Beijing 100072, China). 68—70

Abstract: Five kinds of coatings have been prepared on the surface of 45CrNi steel plates using laser cladded technique by adding 0, 2.5 wt. %, 5 wt. %, 7.5 wt. % and 10 wt. % Mo into the NiCrBSi alloys. The effect of molybdenum on the crack sensibilities of laser cladded NiCrBSi alloy coatings of these five kinds of coatings were investigated by oil whitening test. Crack sensibilities are affected by the coefficient of thermal expansion of the coatings and the solidification characteristics and microstructures. The research results present that NiCrBSi alloy is very sensitive to cracking and many transverse macro cracks appear on the clad pass. While the sizes of dendrites and the carbides morphologies of eutectic microstructure of the coating with 5.0 wt. % of Mo are different from the others. Meanwhile the coefficient of thermal expansion of the coating is decreased. Both of two effects are responsible for the reduction of crack sensibilities.

Key words: laser cladded; crack sensibility; coefficient of thermal expansion; NiCrBSi alloy

Primary study of laser-MIG hybrid welding for MB8 magnesium alloy

GAO Ming, ZENG Xiaoyan, LIN Tianxiao, YAN Jun (Wuhan National Laboratory for Optoelectronics, Huazhong University of Science and Technology, Wuhan 430074, China). p71—74

Abstract: Laser-MIG hybrid welding for MB8 magnesium alloy with 10 mm thickness was carried out and the process stability, appearance of weld, microstructure and tensile strength were studied. The results demonstrate laser MIG hybrid welding is an effective welding method for MB8 magnesium alloy. By the laser-arc interaction, the stabilities of MIG arc burning and droplet transfer are improved during hybrid welding and the obtained weld is full and even. Under the used welding parameters, hybrid welding increases the welding speed by 125 % in comparison of single laser welding. Because of the disappearance of surface pit defect, the tensile strength of hybrid weld is far higher than that of laser weld and reaches 87.2% of substrate. For the hybrid weld, the microstructure in the center of fusion zone is equiaxed grain but that nearby fusion line is columnar grain. Owing to relatively slow solidification speed, the wide upper part has obvious coarser grain size than the narrow lower part.